Charge distribution in U1-xCexO2+y nanoparticles

Prieur, D.; Vigier, J.-F.; Popa, K.; Walter, O.; Dieste, O.; Varga, Z.; Beck, A.; Vitova, T.; Scheinost, A.; Martin, P.;

Originally published:

September 2021

Inorganic Chemistry 60(2021)19, 14550-14556

DOI: https://doi.org/10.1021/acs.inorgchem.1c01071

Charge distribution in $U_{1-x}Ce_xO_{2+y}$ nanoparticles

Damien Prieur[1,2], Jean-François Vigier[3*], Karin Popa[3], Olaf Walter[3], Oliver Dieste[3], Zsolt Varga[3], Aaron Beck[4], Tonya Vitova[4], Andreas C. Scheinost[1,2], Philippe Martin[5]*

[1] Helmholtz Zentrum Dresden-Rossendorf (HZDR), Institute of Resource Ecology, PO Box 510119, 01314 Dresden, Germany.

[2] The Rossendorf Beamline at ESRF—The European Synchrotron, CS40220, 38043 Grenoble Cedex 9, France

[3] European Commission, Joint Research Centre, P.O. Box 2340, 76125 Karlsruhe, Germany.

[4] Institute for Nuclear Waste Disposal, Karlsruhe Institute of Technology, P.O. Box 3640, 76021 Karlsruhe, Germany.

[5] CEA, DEN, DMRC, SFMA, LCC, F30207 Bagnols sur Cèze cedex, France.

ABSTRACT

In view of a safe management of the nuclear wastes, a sound knowledge of the atomic-scale properties of $U_{1-x}M_xO_{2+y}$ nanoparticles is essential. In particular, their cation valences and oxygen stoichiometries are of great interest as these properties drive their diffusion and migration behaviour into the environment. Here, we present an in-depth study of $U_{1-x}Ce_xO_{2+y,}$ over the full compositional domain, by combining XRD and HERFD-XANES. We show on one hand the co-existence of U^{IV}, U^{V} and U^{VI} and on the other hand that the fluorite structure is maintained despite this charge distribution.

KEYWORDS: Uranium, UO_2, CeO_2, HERFD-XANES

INTRODUCTION

The safety assessment of nuclear waste management requires a sound understanding of the corrosion behaviour of the spent nuclear fuel (SNF). Considering that Ce is among the major fission products present in the SNF, which can be incorporated into the UO_2 structure, the crystallography of the present chemical phases and the oxidation states of both U and Ce have to be studied as they drive the concomitant release and migration of $U_{1-x}Ce_xO_{2+y}$ nanoparticles (NPs) in the environment [1,2].

Due to their structural similarity, Uranium and cerium dioxide form solid solution covering the full compositional range of Ce content [3–5]. Several articles have been published on the $U_{1-x}Ce_xO_{2+y}$ properties (electrical conductivity, magnetic properties, oxygen potential, lattice parameter, heat capacity, thermal expansion, phase diagram and) [6–8,3,9,10]. Some interesting results have also been reported on both U and Ce valences. Contrary to other substituted-UO_2 compounds[11–13], no charge transfer reaction between U^{IV} and Ce^{IV} leading to the formation Ce^{III} and U^{V} has been reported. Indeed, when the mixed oxide are prepared in the right oxygen potential condition to obtain stoichiometric compounds $U_{1-x}Ce_xO_{2.00}$, their lattice parameters follow closely the Vergard's law [8,14], suggesting the progressive substitution of U^{IV} by Ce^{IV} cation as a function of the composition. Even though there have been several investigation on the redox behaviour of Ce doped-UO_2 mainly on thin films using extreme surface sensitive technics [6,7,15], there is none for NP materials. However, in those latter compounds, the quantum mechanical size effects, combined with a considerable increase of the surface to bulk ratio, may affect the local structure and the charge

distribution within the compounds[16–18]. Additionally, NPs are highly sensitive to room temperature oxidation as they show a considerable surface to bulk ratio [19].

In this context, the present study aims at studying both U and Ce valences in room temperature oxidized $U_{1-x}Ce_xO_{2+y}$ NPs. The crystal structure of both as-synthesized and room temperature oxidized $U_{1-x}Ce_xO_{2+y}$ NPs was characterized using x-ray diffraction (XRD), giving access to their size and lattice parameter. Furthermore, we probed the electronic structure of the $U_{1-x}Ce_xO_{2+y}$ NPs using high-energy resolution fluorescence-detection hard X-ray absorption near-edge structure (HERFD-XANES) spectroscopy at both U M_{IV} and Ce L_{III} edges.

EXPERIMENTAL METHODS

Please note that a careful attention should be made for the characterization of these nanocrystalline materials to avoid any energy-induced transformations (such as reduction under beam for instance). It has to be mentioned that these materials are radioactive and hence should be manipulated adequately.

Synthesis

The $U_{1-x}Ce_xO_{2+y}$ nanopowders were produced by the decomposition of mixed hydroxides under hot compressed water. $U_{1-x}Ce_x(OH)_4$ (x=0-1) amorphous precipitates were prepared as followings: *2-2x* ml U^{IV} solution (0.5 M) and *2x* ml Ce^{IV} solution (0.5 M) were mixed in test tubes of 50 ml and diluted with 8 ml of distilled water. The coprecipitation was induced with excess (10 ml) of ammonia solution 25% (pH=14). The precipitates were separated from the alkaline solution and washed repeatedly with distilled water till neuter pH. After washing, the hydroxides precipitates were inserted in Teflon lined hydrothermal synthesis autoclave reactors together with 10 ml

distilled water and reacted for 4 h at 200 ºC and 15 bar without stirring. The final product consists (usually) in nanocrystalline $U_{1-x}Ce_xO_{2+y}$ solid solutions which could be easily separated from solution. The nanocrystals were repeatedly washed with ethanol and acetone in order to remove the water potentially absorbed at the surface. Finally, they were dried under air atmosphere.

The hydroxide decomposition method under hot compressed water proved to be straightforward in the case of CeO_2, ThO_2 and $U_{1-x}Th_xO_2$ solid solutions[20,21,16,22]. However, the preparation of $U_{1-x}Ce_xO_{2+y}$ solid solutions through this synthetic route is not always successful and the method still needs optimisation. Thus, we have observed (meta)schoepite-like impurities in more than half of the experimental trials, independent on the targeted composition. Potentially different reaction intermediates are formed in this specific case, but the mechanistic study is out of our scope.

The U:Ce ratio (i.e. the stoichiometry) was measured by a NuPlasma™ (NU Instruments, Oxford, United Kingdom) double-focusing multi-collector inductively coupled plasma mass spectrometer (MC-ICP-MS). U and Ce monoelemental solutions were used for the calibration of the instrument. For the dissolution, a small amount of the sample was dissolved in 8 M HNO_3, then successively diluted before the MC-ICP-MS measurement. All dilutions were performed gravimetrically. The results have +/-5% relative uncertainty.

The synthetic procedure was performed under an air atmosphere in a fumehood. The products were stored in a desiccator under vacuum, after flushing with argon.

X-ray diffraction

Due to the fast oxidation of the resulting powders, preliminary XRD analyses were performed with a Rigaku Miniflex 600 diffractometer at the same day of the synthesis. The diffractometer is calibrated with silicon, use Cu K_α radiation (both $K_{\alpha1}$ and $K_{\alpha2}$) and is operated under air. The

crystallite size of the nanopowders was estimated from the XRD pattern using the Scherrer equation and averaging the results of 8 selected peaks in the 2θ range between 25 and 80°.

The other measurements (done 2 weeks and 3 months after synthesis) used for Rietveld refinement were performed using room temperature XRD analyses performed on about 10 mg of powder with a Bruker D8 Advance diffractometer (Cu K_α radiation, 40 kV, 40 mA) mounted in a Bragg-Brentano configuration. The diffractometer was equipped with a curved Ge (111) Kα1 monochromator, a ceramic copper tube and a LinxEye position sensitive detector. It is calibrated with LaB6 reference material (NIST SMR 660b). The diffractometer is installed in a Nitrogen atmosphere glovebox, designed to handle highly radiotoxic materials.

With both diffractometers, the XRD patterns were recorded using a step size of 0.02° across the $10° \leq 2\theta \leq 120°$ angular range. Structural analysis was performed by the Rietveld method using the Jana2006 software[23].

Transmission Electron Microscopy

Transmission electron microscopy (TEM) studies were performed using an aberration (image) corrected FEI™ Titan 80-300 operated at 300 kV. This provides a nominal information limit of 0.8 Å in TEM mode and a resolution of 1.4 Å in STEM mode. TEM micrographs have been recorded using a Gatan US1000 slowscan CCD camera. STEM images have been recorded using a Fischione high-angle annular dark-field (HAADF) detector with a camera length of 195 mm. The samples for analysis have been prepared by dropping coating with a suspension of the nanoparticles in ultrapure water on carbon coated copper grids.

High-Energy Resolution Fluorescence-Detected X-ray Absorption Near Edge Structure

Inner-shell spectroscopy with the use of an X-ray emission spectrometer provides an element-selective probe of the electronic state and allows observing spectral features with significantly enhanced energy resolution compared to usual data limited by the core-hole life-time broadening [16,24].

HERFD-XANES measurements were conducted at the CAT-ACT beamline (ACT station) of the KIT synchrotron light source (Karlsruhe Institute of Technology, Karlsruhe, Germany) [25,26]. The storage ring conditions were 2.5 GeV and 160 mA. Note that those were carried out 3 months after the synthesis. The incident energy was selected using the [111] reflection of a double Si crystal monochromator. The X-ray beam was focused to 1×1 mm onto the sample. A slit with a size of 500x500 µm was used in front of the sample, in order to further confine the size of the X-ray beam on the sample, leading to a slight improvement of the energy resolution. XANES spectra were measured in high-energy-resolution fluorescence detected (HERFD) mode using an X-ray emission spectrometer[24,27]. The sample, analyzer crystal, and a single diode VITUS Silicon Drift Detector (KETEK, Germany) were arranged in a vertical Rowland geometry.

The Ce L_{III} HERFD-XANES spectra were obtained by recording the maximum intensity of the Ce L_3-M_5 emission line (4839 eV) as a function of the incident energy. The emission energy was selected using the ⟨331⟩ reflection of four spherically bent Ge crystal analyser (with a bending radius R = 1 m) aligned at 80.7° Bragg angle. The molar fractions of Ce^{III} and Ce^{IV} were derived from the linear combination of CeO_2 and Ce^{III} oxalate references [16].

The U M_{IV} HERFD-XANES were acquired by recording the intensities of the U M_4-N_6 (~3337 eV) as a function of the incident energy. The emission energy was selected using the (220) reflection of four spherically bent Si crystal analyzers (with 1 m bending radius) aligned at 75.4° Bragg angle. The molar fractions of U^{IV}, U^{V} and U^{VI} were derived from the linear combination of UO_2, U_4O_9, U_3O_8, UO_3 and $U_{0.50}Am_{0.50}O_{2-y}$ references[28,29].

The experimental energy resolutions were 1.15 eV and 0.85 eV for Ce L_{III} and U M_{IV}, respectively. Those were obtained by measuring the FWHM of the elastically scattered incident beam.

The sample, crystals and detector were set in a box filled with He. A constant He flow was maintained in order to minimize the loss of intensity due to absorption and scattering of the X-rays. The data were not corrected for self-absorption effects. The sample exposure to the beam was minimized to account for possible beam damage and checked by first collecting short XANES scans (~10 seconds) to look for irradiation effect.

RESULTS AND DISCUSSION

Lattice parameter and size of the as-synthesized NPs

XRD measurements were carried out a few hours after the synthesis.

Our XRD data show that the as-synthesized $U_{1-x}Ce_xO_{2+y}$ crystallize in the Fm-3m fluorite structure (space group 225). Depending on the Ce content, the average crystallite diameters vary from 5 to 13 nm. These XRD-refined parameters are gathered in the Table 3**.**

Table 1: Lattice parameter, space group and crystallite size derived from the Rietveld refinement.

	Lattice parameter (Å)	Space group	Crystallite size (nm)
$U_{0.90}Ce_{0.10}O_{2+y}$	5.460(2)	Fm-3m	13(1.2)
$U_{0.60}Ce_{0.40}O_{2+y}$	5.446(2)	Fm-3m	7.1(0.9)
$U_{0.50}Ce_{0.50}O_{2+y}$	5.441(2)	Fm-3m	7.3(1.0)
$U_{0.40}Ce_{0.60}O_{2+y}$	5.428(2)	Fm-3m	7.1(1.0)
$U_{0.17}Ce_{0.83}O_{2+y}$	5.417(2)	Fm-3m	7.0(0.9)
$U_{0.10}Ce_{0.90}O_{2+y}$	5.413(2)	Fm-3m	5.1(0.6)

The TEM measurements confirm the XRD data with respect of both phase purity and particle size. As a representative example, the Figure 1 shows the morphology of the nanometric $U_{0.50}Ce_{0.5}O_{2+y}$ sample, which is clearly formed by one single family of particles with an average size of 7.3 (1.8) nm. Moreover, EDX analysis on independent particles has confirmed the homogeneity of all the samples as well as their U:Ce ratio.

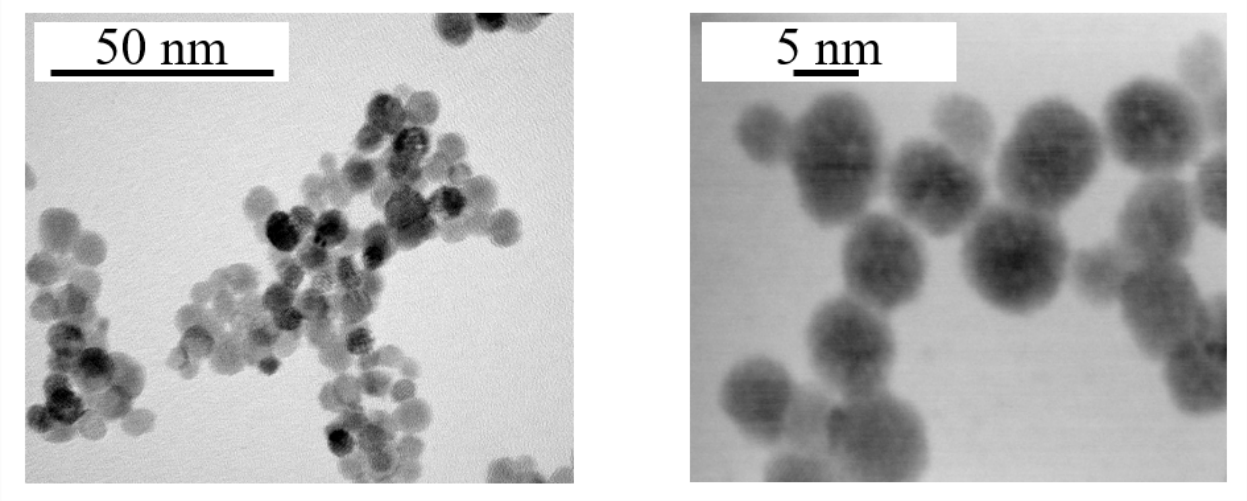

Figure 1: TEM images of the as-synthesized $U_{0.50}Ce_{0.50}O_{2+y}$.

As it can be expected from the literature data[7,30–33], the Figure 7 shows that the lattice parameters of the as-synthesized compounds follow the UO_2-CeO_2 Vegard law. Although the charge distribution has not been measured for these NPs, one can expect that the oxygen stoichiometry or O/M (with M=U+Ce) ratio is equal to 2.00 or very close to these value. The principle of electroneutrality implies that either Ce and U are both tetravalent or that Ce^{III} and U^{V} co-exist in equimolar proportions, as it has been demonstrated in other doped UO_2 compounds[11–13]. It is very interesting to notice that, despite the formation of nanoparticles having a very high surface area, and the use of water in the synthesis method, the conditions are obviously reductive enough to obtain close to stoichiometric materials. However, as presented in the next section, these particles stay very sensitive to the oxidation, and their oxidation actually take place in the following days despite the storage of the sample in nitrogen glove boxes.

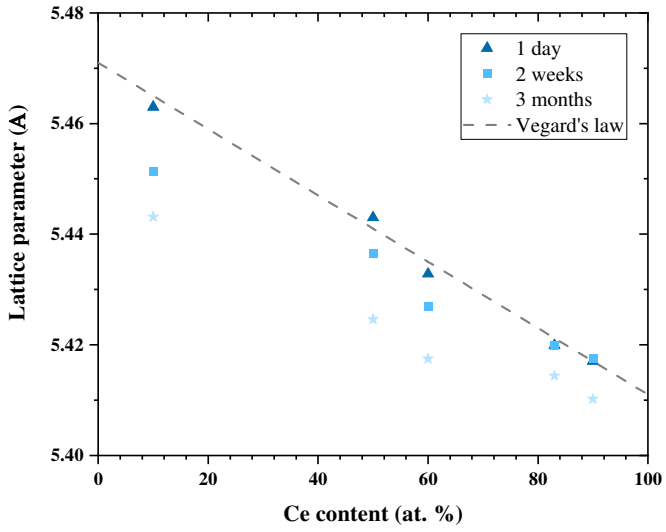

Figure 2: Lattice parameters as a function of Ce content. The lattice parameters of the as-synthesized compounds follows the Vegard's law law (drawn from pure $UO_{2.00}$ and $CeO_{2.00}$ values)

while an evolution in time is observed for those collected 1 day, 2 weeks, 3 months after the synthesis

Evolution of the NPs lattice parameter

The $U_{1-x}Ce_xO_{2+y}$ NPs were stored in a desiccator under vacuum, after flushing with argon during 3 months before the HERFD-XANES measurement. During this period, XRD measurements were regularly performed to assess the evolution of their lattice parameters.

As a general trend, we can see on the Figure 7 that the lattice parameter decreases with time for each composition. This evolution of the unit cell is characteristic of an oxidation process [34], which is besides in perfect agreement with the very high specific area of the studied NPs. Considering the oxidation mechanism in UO_2 [35,36], one can assume here that U^{IV} have been oxidized into higher valence states in agreement with O/M ratio greater than 2.00. The charge distribution of these 3 months – stored NPs have been assessed using HERFD-XANES.

Charge distribution of the room temperature oxidized NPs

Ce oxidations state

The Ce L_{III} HERFD-XANES spectra of all the investigated $U_{1-x}Ce_xO_{2+y}$ NPs, as well as Ce^{III} and Ce^{IV} references, are given in Figure 8 and compared with CeO_2 and Ce^{III} references.

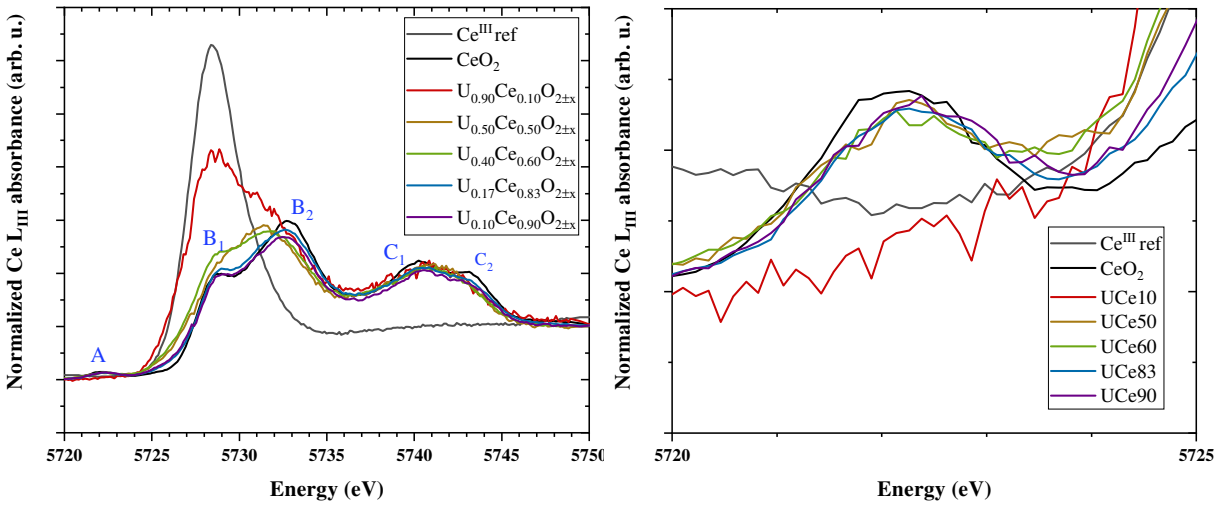

Figure 3: (Left) Ce L_{III} HERFD-XANES spectra of $U_{1-x}Ce_xO_{2+y}$ NPs compared to CeO_2 reference. (Right) Pre-edge region of the Ce L_{III} HERFD-XANES spectra.

Three characteristic features (A, B and C) are observed on the HERFD-XANES spectrum of bulk CeO_2. The pre-edge peak (noted A) originates from the 2p transition to a mixed 5d-4f band/orbital/state. A doublet structure, due to the crystal field splitting of 5d states[37], is observed for screened B (B1+B2) and unscreened C (C1+C2) excited states.[38,39]. These arises from transitions from $2p_{3/2} \rightarrow 5d_{5/2}$ transitions.

In contrast, the HERFD-XANES spectrum of the bulk Ce^{III} reference shows only one single feature.

Regarding the HERFD-XANES spectra of the $U_{1-x}Ce_xO_{2+y}$ NPs, one can observe that the spectra are quite similar in the 5735 eV – 5750 eV region, corresponding to the C (C1+C2) feature of the CeO_2 reference. One can then argue that this C doublet is not affected by the Ce oxidation state but mostly by the local structure (as the crystallographic structure remains the same for all compounds). However, strong differences can be observed in the 5720 eV – 5735 eV range,

corresponding to the A and B feature of the CeO_2 reference. In the case of $U_{0.90}Ce_{0.10}O_{2\pm x}$, the Ce L_{III} threshold is strongly shifted toward lower energy, and one maximum is observed at the same energy as the Ce^{III} reference. For both $U_{0.50}Ce_{0.50}O_{2+y}$ and $U_{0.40}Ce_{0.60}O_{2+y}$ samples, the spectra look quite similar and can be compare to the shape of the CeO_2 reference, although the B_1 and B_2 positions are shifted toward lower energy. For the $U_{0.17}Ce_{0.83}O_{2+y}$ and $U_{0.10}Ce_{0.90}O_{2+y}$, the spectra exhibit the same shape as the CeO_2 reference.

The Ce^{III} and Ce^{IV} molar fractions deduced from Ce L_{III} HERFD-XANES are provided in **Error! Reference source not found.**.

Table 2: U and Ce valences, molar fractions and O/M ratios derived from the fitting of the U M_{IV} and Ce L_{III} HERFD-XANES spectra. * U_{surf} corresponds to the fraction of U atoms at the surface of the NPs. This fraction was derived taking into account the lattice parameter and the NP size.

	U^{IV} (%)	U^{V} (%)	U^{VI} (%)	Valence of U	Ce^{III} (%)	Ce^{IV} (%)	Valence of Ce	O/M	U_{surf} * (%)
$U_{0.90}Ce_{0.10}O_{2+y}$	38 (5)	57 (5)	5 (5)	4.67	60 (5)	40 (5)	3.6	2.28 (1)	12
$U_{0.50}Ce_{0.50}O_{2+y}$	9 (5)	50 (5)	41 (5)	5.33	14 (5)	86 (5)	3.86	2.25 (1)	22
$U_{0.40}Ce_{0.60}O_{2+y}$	5 (5)	39 (5)	56 (5)	5.51	13 (5)	87 (5)	3.87	2.26 (1)	22
$U_{0.17}Ce_{0.83}O_{2+y}$	3 (5)	31 (5)	66 (5)	5.64	0	100 (5)	4	2.13 (1)	22

$U_{0.10}Ce_{0.90}O_{2+y}$	3 (5)	31 (5)	66 (5)	5.62	0	100 (5)	4	2.08 (1)	29

In addition, some papers [40] recommend using the Ce L_{III} pre-edge to assess the molar fractions of Ce^{III} and Ce^{IV}. However, in our present work, the pre-edges of all of our NPs have both similar shape, amplitude and position while the features above the edge are clearly different. This shows that a proper determination of the Ce valence can only be achieved fitting the edge region.

U oxidation state

The oxidation state and electronic structure of U was assessed using U M_{IV} edge HERFD-XANES. The corresponding spectra of each NP sample compared to $U^{IV}O_{2.00}$ and $(U^{V}_{0.67}U^{VI}_{0.33})_3O_8$ references [28] are provided in the Figure 9.

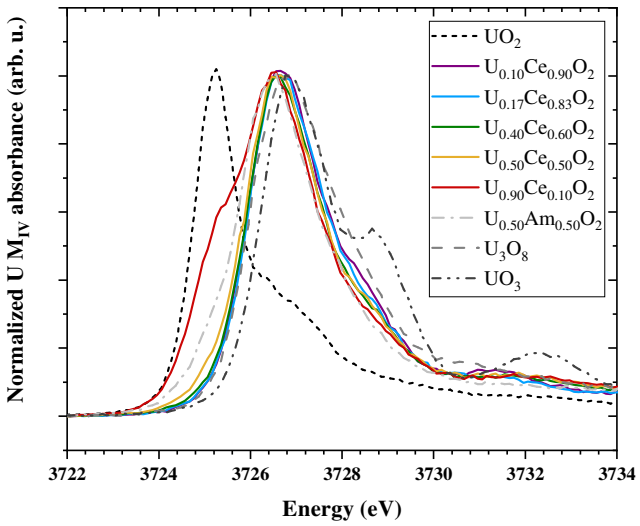

Figure 4: U M_4 HERFD-XANES spectra of $U_{1-x}Ce_xO_{2+y}$ NPs compared to UO_2, U_3O_8, UO_3 and $U_{0.50}Am_{0.50}O_2$ references.

As previously reported [41,28,42–45,11,36,46,35], the various oxidations states of U are perfectly identifiable at M_{IV} edges. The HERFD-XANES spectrum of $U^{IV}O_2$ shows a sharp peak at 3725.2 (2) eV, resulting from the transition from the $3d_{5/2}$ core level to the unoccupied $5f_{5/2}$ levels. The $(U^{IV}_{0.5}U^{V}_{0.5})_4O_9$ HERFD-XANES spectrum presents this U^{IV} characteristic feature as well as a peak at 3726.2 (2) eV corresponding to U^{V}. In the case of $(U^{V}_{0.67}U^{VI}_{0.33})_3O_8$, the HERFD-XANES spectrum exhibit a white line at 3726.9 (2) eV attributed to U^{VI}. At the lower energy side, a shoulder is observed, which energy matches the same position as the characteristic feature of U^{V} in $(U^{IV}_{0.5}U^{V}_{0.5})_4O_9$ [28].

Except the $U_{0.90}Ce_{0.10}O_{2+y}$ U M_{IV} HERFD-XANES spectrum, all the others spectra are ranging between the U_4O_9 and U_3O_8 reference spectra. Their white line shapes are close to U_3O_8 although various intensities of the U^{V} and U^{VI} features are observed, suggesting varying fractions of this species. Also, one should note that the presence of U^{IV} is also clearly evidenced by its 3725.2 (2) eV feature. For $U_{0.90}Ce_{0.10}O_{2+y}$ NP, one can clearly observe a shoulder at the left side which is at the same position as the peak characteristic of U^{IV} in $U^{IV}O_2$, which confirms the presence of U^{IV}.

Charge distribution

From the assessed molar fractions of Ce and U provided in the Table 2, it is clear that the U and Ce valences are proportional. Those oxidations states increase with the Ce content. For the higher content of Ce, the main valence states are U^{V}, U^{VI} and Ce^{IV}. For all NPs, hyper-stoichiometric materials are achieved. This is in good agreement with the strong decrease of the lattice parameter compared to the values measured on the as-synthesized compounds and with the values of ionic radius [47]. We can then assume that after the synthesis the NPs were nearly stoichiometric (as the

lattice parameter are matching the Vegard's law) and then oxidize during the next 3 months with the oxidation of U^{IV} into U^{V} and U^{VI}.

Presence of U^{VI} within the fluorite structure

The presence of U^{VI} has already been reported in $U_{1-x}Ce_xO_{2+y}$ thin films, but the nature of the U^{VI} phase is not discussed in this paper [15]. In Ln^{III} [48–50] and Am[51] doped UO_2 compounds, U^{VI} was also evidenced and attributed to the presence of $(U,M)_3O_8$ phase. For $U_{1-x}Bi_xO_{2+y}$ materials, no evidence of such $(U,M)_3O_8$ phase was found and hence U^{VI} was assumed to crystallize in the fluorite structure[43,52]. In the present work, only fluorite solid solutions are derived from XRD and no $(U,Ce)_3O_8$ is detected. Considering that we work in presence of NPs and with bulk+surface-sensitive techniques, we could assume that the molar fraction of U^{VI} in our NPs solely originates from the presence of surface species. However, except the $U_{0.90}Ce_{0.10}O_{2+y}$, the Table 2 shows that the number of U atoms at the surface is always lower than the U^{VI} molar fraction, which means that U^{VI} co-exist with U^{IV} and U^{V} within the fluorite-structured bulk.

Co-existence of U^{IV}, U^{V} and U^{VI} within the fluorite structure

The co-existence of several U oxidation states in the doped UO_2 fluorite structure has already been evidenced. Indeed, it was shown that the incorporation of non-tetravalent cation in the UO_2 structure is accommodated through the formation of U^{V} in $U_{1-x}Am_xO_2$, $U_{1-x}La_xO_2$, $U_{1-x}Bi_xO_2$ and $U_{1-x}Gd_xO_2$ in the range $0 < x_M < 0.50$ [11,12,43,52]. Doping with a trivalent cation results hence in the oxidation of U^{IV} into U^{V}. Remarkably, equimolar fractions of M^{III} and U^{V} were often measured leading to oxygen stoichiometry very close equal to 2.00. However, for $0.40 \leq x_{Am} \leq 0.70$, this charge compensation mechanism is no longer sufficient as the molar fraction of U^{V} becomes higher

than that of Am^{III} and, for even higher Am content, Am^{III} starts oxidizing into Am^{IV}. These variations of the average oxidation state (AOS) of U and Am in $U_{1-x}Am_xO_2$ are given in green in the Figure 10 as a function of the M content. On this plot, the AOS of Ce and U determined in this work are also presented in blue. Overall, the tendency between $U_{1-x}Am_xO_2$ and $U_{1-x}Ce_xO_2$ NPs is similar, meaning that both U and M AOS are proportional to the M content. Even if the two systems shows significant differences in term of valence ratio, probably due to the difference of Am^{III} and Ce^{III} stability in oxides, it is interesting to see the similarity between the two systems. Indeed, at high uranium content ($0.50 \leq x_{Am}$), Am^{III} is fully stabilised in the $U_{1-x}Am_xO_{2\pm x}$ system, and this even after air oxidation at high temperature [53]. Similarly here, the Ce^{III} is partially stabilised in the $U_{1-x}Ce_xO_{2\pm x}$ system, especially for low cerium content, and this despite the room temperature oxidation of the nanoparticles over the time.

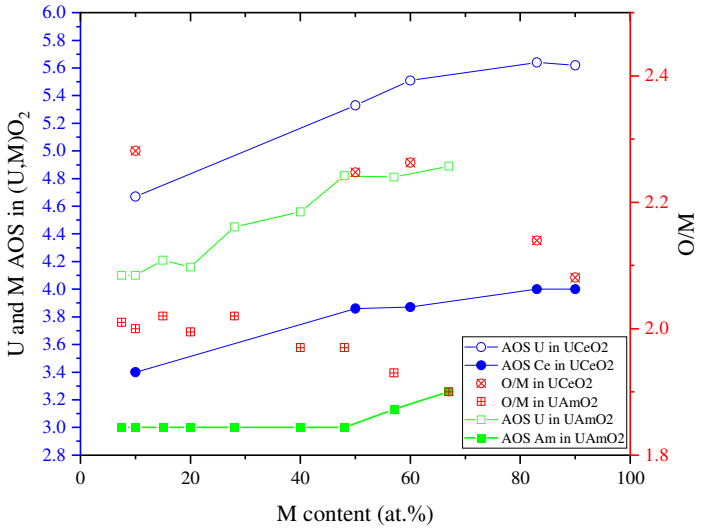

Figure 5: (Left axis) U and M average oxidation states and (Right axis) O/M as a function of the M content in $U_{1-x}Ce_xO_{2+y}$ and $(U,Am)O_{2+y}$.

FIGURES

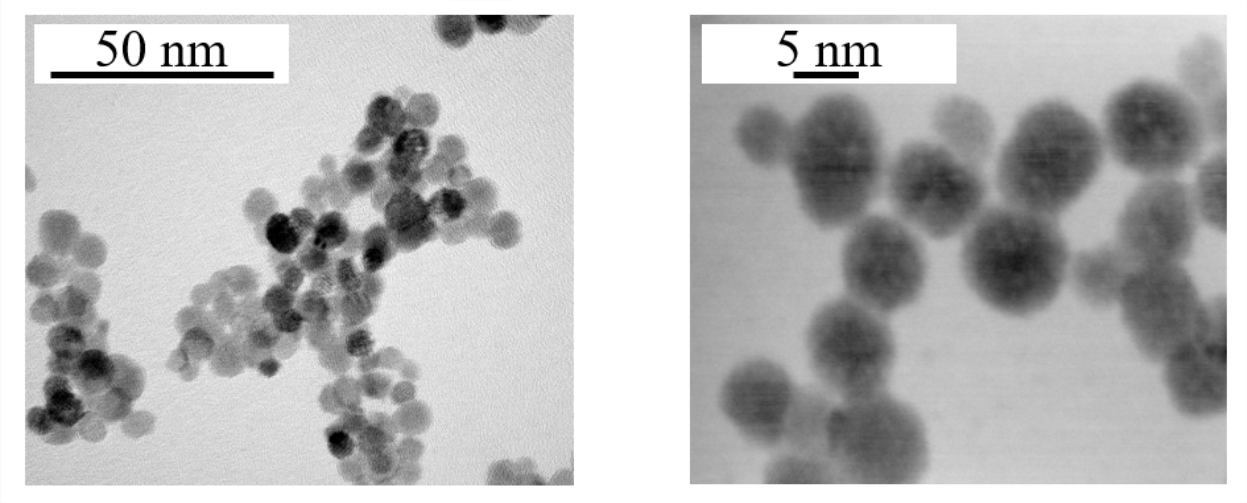

Figure 6: TEM images of the as-synthesized $U_{0.50}Ce_{0.50}O_{2+y}$.

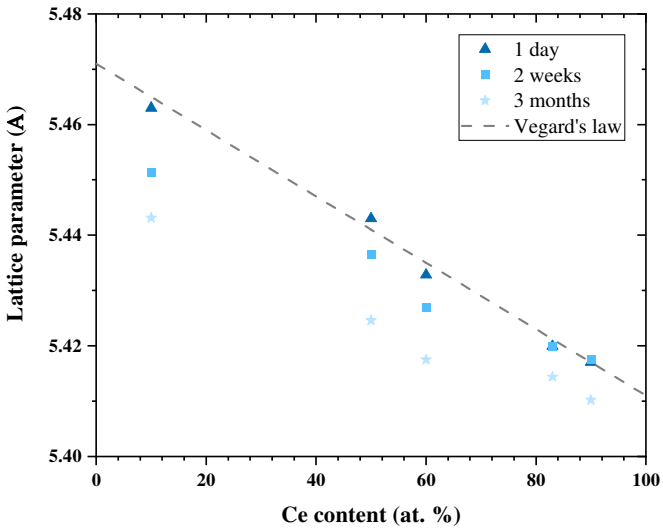

Figure 7: Lattice parameters as a function of Ce content. The lattice parameters of the as-synthesized compounds follows the Vegard's law law (drawn from pure $UO_{2.00}$ and $CeO_{2.00}$ values) while an evolution in time is observed for those collected 1 day, 2 weeks, 3 months after the synthesis

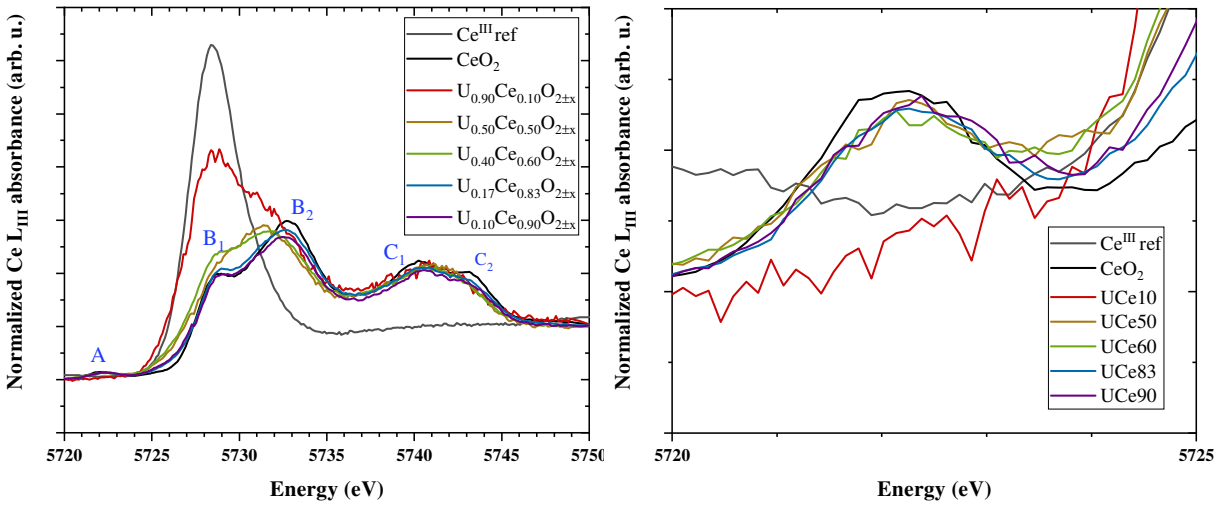

Figure 8: (Left) Ce L_{III} HERFD-XANES spectra of $U_{1-x}Ce_xO_{2+y}$ NPs compared to CeO_2 reference. (Right) Pre-edge region of the Ce L_{III} HERFD-XANES spectra.

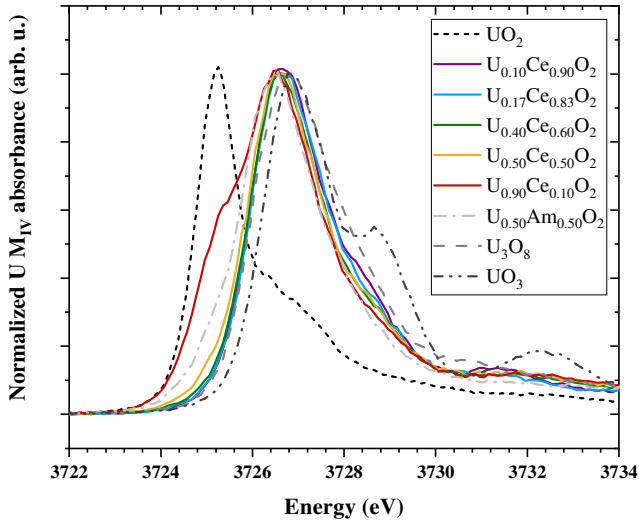

Figure 9: U M_4 HERFD-XANES spectra of $U_{1-x}Ce_xO_{2+y}$ NPs compared to UO_2, U_3O_8, UO_3 and $U_{0.50}Am_{0.50}O_2$ references.

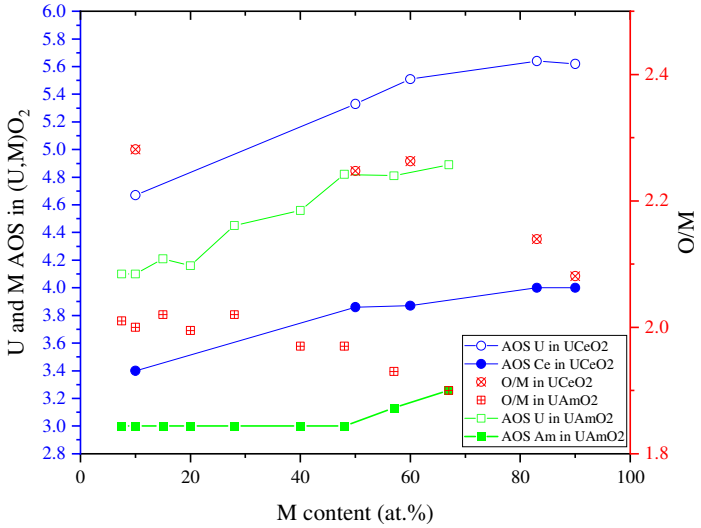

Figure 10: (Left axis) U and M average oxidation states and (Right axis) O/M as a function of the M content in $U_{1-x}Ce_xO_{2+y}$ and $(U,Am)O_{2+y}$.

TABLES

Table 3: Lattice parameter, space group and crystallite size derived from the Rietveld refinement.

	Lattice parameter (Å)	Space group	Crystallite size (nm)
$U_{0.90}Ce_{0.10}O_{2+y}$	5.460(2)	Fm-3m	13(1.2)
$U_{0.60}Ce_{0.40}O_{2+y}$	5.446(2)	Fm-3m	7.1(0.9)
$U_{0.50}Ce_{0.50}O_{2+y}$	5.441(2)	Fm-3m	7.3(1.0)
$U_{0.40}Ce_{0.60}O_{2+y}$	5.428(2)	Fm-3m	7.1(1.0)
$U_{0.17}Ce_{0.83}O_{2+y}$	5.417(2)	Fm-3m	7.0(0.9)
$U_{0.10}Ce_{0.90}O_{2+y}$	5.413(2)	Fm-3m	5.1(0.6)

Table 4: U and Ce valences, molar fractions and O/M ratios derived from the fitting of the U M_{IV} and Ce L_{III} HERFD-XANES spectra. * U_{surf} corresponds to the fraction of U atoms at the surface of the NPs. This fraction was derived taking into account the lattice parameter and the NP size.

	U^{IV} (%)	U^{V} (%)	U^{VI} (%)	Valence of U	Ce^{III} (%)	Ce^{IV} (%)	Valence of Ce	O/M	U_{surf} * (%)
$U_{0.90}Ce_{0.10}O_{2+y}$	38 (5)	57 (5)	5 (5)	4.67	60 (5)	40 (5)	3.6	2.28 (1)	12
$U_{0.50}Ce_{0.50}O_{2+y}$	9 (5)	50 (5)	41 (5)	5.33	14 (5)	86 (5)	3.86	2.25 (1)	22
$U_{0.40}Ce_{0.60}O_{2+y}$	5 (5)	39 (5)	56 (5)	5.51	13 (5)	87 (5)	3.87	2.26 (1)	22
$U_{0.17}Ce_{0.83}O_{2+y}$	3 (5)	31 (5)	66 (5)	5.64	0	100 (5)	4	2.13 (1)	22
$U_{0.10}Ce_{0.90}O_{2+y}$	3 (5)	31 (5)	66 (5)	5.62	0	100 (5)	4	2.08 (1)	29

AUTHOR INFORMATION

Corresponding Authors

*E-mail: d.prieur@hzdr.de; E-mail jean-françois.vigier@ec.europa.eu

Author Contributions

K.P. and O.W. carried out the NPs synthesis work. J-F.V, K.P., O.W., O.D.B. and Z.V. performed characterizations of the samples using in-house laboratory equipment. D.P. and P.M performed synchrotrons measurements and associated data treatment. K.D., J.R., A.B. and T.V. set up the spectrometer for U M_{IV} and Ce L_{III} measurements. D.P., J-F.V., K.P. and P.M. co-wrote the paper. D.P., K.P., P.M., O.W. and A.C.S. were involved in planning and supervision of the work. All authors discussed the results and contributed to the final manuscript.

Conflicts of interest

There are no conflicts to declare.

ACKNOWLEDGMENT

D. P., P.M., K.P. and O.W. acknowledge the KIT light source for provision of instruments at their beamlines and the Institute for Beam Physics and Technology (IBPT) for the operation of the storage ring, the Karlsruhe Research Accelerator (KARA). K.P., W.B. and O.W. acknowledge Daniel Bouëxière, Antony Guiot and Herwin Hein for the technical support.

REFERENCES

(1) Piro, M. H. A.; Dumas, J.-C.; Lewis, B. J.; Thompson, W. T.; Iglesias, F. C. 2.07 - Fission Product Chemistry in Oxide Fuels☆. In *Comprehensive Nuclear Materials (Second Edition)*; Konings, R. J. M., Stoller, R. E., Eds.; Elsevier: Oxford, 2020; pp 173–199. https://doi.org/10.1016/B978-0-12-803581-8.12048-X.

(2) Plakhova, T. V.; Romanchuk, A. Yu.; Yakunin, S. N.; Dumas, T.; Demir, S.; Wang, S.; Minasian, S. G.; Shuh, D. K.; Tyliszczak, T.; Shiryaev, A. A.; Egorov, A. V.; Ivanov, V. K.; Kalmykov, S. N. Solubility of Nanocrystalline Cerium Dioxide: Experimental Data and Thermodynamic Modeling. *J. Phys. Chem. C* **2016**, *120* (39), 22615–22626. https://doi.org/10.1021/acs.jpcc.6b05650.

(3) Batuk, O. N.; Szabó, D. V.; Denecke, M. A.; Vitova, T.; Kalmykov, S. N. Synthesis and Characterization of Thorium, Uranium and Cerium Oxide Nanoparticles. *Radiochimica Acta International journal for chemical aspects of nuclear science and technology* **2013**, *101* (4), 233–240. https://doi.org/10.1524/ract.2012.2014.

(4) Maji, D.; Ananthasivan, K.; Venkata Krishnan, R.; Balakrishnan, S.; Amirthapandian, S.; Joseph, K.; Dasgupta, A. Nanocrystalline (U0.5Ce0.5)O2±x Solid Solutions through Citrate Gel-Combustion. *J. Nucl. Mater.* **2018**, *502*, 370–379. https://doi.org/10.1016/j.jnucmat.2017.10.007.

(5) Maji, D.; Ananthasivan, K.; Venkatakrishnan, R.; Desigan, N.; Pandey, N. K. Synthesis, Characterization and Sintering of Nanocrystalline (U1-YCey)O2±x. *J. Nucl. Mater.* **2021**, *547*, 152824. https://doi.org/10.1016/j.jnucmat.2021.152824.

(6) Nagarajan, K.; Saha, R.; Yadav, R. B.; Rajagopalan, S.; Kutty, K. V. G.; Saibaba, M.; Rao, P. R. V.; Mathews, C. K. Oxygen Potential Studies on Hypostoichiometric Uranium-Cerium

Mixed Oxide. *J. Nucl. Mater.* **1985**, *130*, 242–249. https://doi.org/10.1016/0022-3115(85)90313-7.

(7) Venkata Krishnan, R.; Nagarajan, K. Heat Capacity Measurements on Uranium–Cerium Mixed Oxides by Differential Scanning Calorimetry. *Thermochimica Acta* **2006**, *440* (2), 141–145. https://doi.org/10.1016/j.tca.2005.11.005.

(8) Venkata Krishnan, R.; Panneerselvam, G.; Singh, B. M.; Kothandaraman, B.; Jogeswararao, G.; Antony, M. P.; Nagarajan, K. Synthesis, Characterization and Thermal Expansion Measurements on Uranium–Cerium Mixed Oxides. *J. Nucl. Mater.s* **2011**, *414* (3), 393–398. https://doi.org/10.1016/j.jnucmat.2011.05.010.

(9) Gasperi, G.; Amidani, L.; Benedetti, F.; Boscherini, F.; Glatzel, P.; Valeri, S.; Luches, P. Electronic Properties of Epitaxial Cerium Oxide Films during Controlled Reduction and Oxidation Studied by Resonant Inelastic X-Ray Scattering. *Phys. Chem. Chem. Phys.* **2016**, *18* (30), 20511–20517. https://doi.org/10.1039/C6CP04407G.

(10) Hofmann, K. A.; Höschele, K. Das Magnesiumchlorid Als Mineralisator. II.: Das Urancerblau Und Das Wesen Der Konstitutiven Färbung. Das Magnesiarot Und Das Magnesiagrün. *Berichte der deutschen chemischen Gesellschaft* **1915**, *48* (1), 20–28. https://doi.org/10.1002/cber.19150480106.

(11) Prieur, D.; Martel, L.; Vigier, J.-F.; Scheinost, A. C.; Kvashnina, K. O.; Somers, J.; Martin, P. M. Aliovalent Cation Substitution in UO2: Electronic and Local Structures of U1–YLayO2±x Solid Solutions. *Inorg. Chem.* **2018**, *57* (3), 1535–1544. https://doi.org/10.1021/acs.inorgchem.7b02839.

(12) Prieur, D.; Martin, P.; Lebreton, F.; Delahaye, T.; Banerjee, D.; Scheinost, A. C.; Jankowiak, A. Accommodation of Multivalent Cations in Fluorite-Type Solid Solutions:

Case of Am-Bearing UO2. *J. Nucl. Mater.* **2013**, *434* (1–3), 7–16. https://doi.org/10.1016/j.jnucmat.2012.11.037.

(13) Prieur, D.; Martin, P. M.; Jankowiak, A.; Gavilan, E.; Scheinost, A. C.; Herlet, N.; Dehaudt, P.; Blanchart, P. Local Structure and Charge Distribution in Mixed Uranium-Americium Oxides: Effects of Oxygen Potential and Am Content. *Inorg. Chem.* **2011**, *50* (24), 12437–12445. https://doi.org/10.1021/ic200910f.

(14) Markin, T. L.; Street, R. S.; Crouch, E. C. The Uranium-Cerium-Oxygen Ternary Phase Diagram. *J. Inorg. Nucl. Chem.* **1970**, *32* (1), 59–75. https://doi.org/10.1016/0022-1902(70)80449-3.

(15) Eloirdi, R.; Cakir, P.; Huber, F.; Seibert, A.; Konings, R.; Gouder, T. X-Ray Photoelectron Spectroscopy Study of the Reduction and Oxidation of Uranium and Cerium Single Oxide Compared to (U-Ce) Mixed Oxide Films. *Appl. Surf. Sci.* **2018**, *457*, 566–571. https://doi.org/10.1016/j.apsusc.2018.06.148.

(16) Prieur, D.; Bonani, W.; Popa, K.; Walter, O.; Kriegsman, K. W.; Engelhard, M. H.; Guo, X.; Eloirdi, R.; Gouder, T.; Beck, A.; Vitova, T.; Scheinost, A. C.; Kvashnina, K.; Martin, P. Size Dependence of Lattice Parameter and Electronic Structure in CeO2 Nanoparticles. *Inorg. Chem.* **2020**. https://doi.org/10.1021/acs.inorgchem.0c00506.

(17) Plakhova, T. V.; Romanchuk, A. Yu.; Likhosherstova, D. V.; Baranchikov, A. E.; Dorovatovskii, P. V.; Svetogorov, R. D.; Shatalova, T. B.; Egorova, T. B.; Trigub, A. L.; Kvashnina, K. O.; Ivanov, V. K.; Kalmykov, S. N. Size Effects in Nanocrystalline Thoria. *J. Phys. Chem. C* **2019**, *123* (37), 23167–23176. https://doi.org/10.1021/acs.jpcc.9b04379.

(18) Amidani, L.; Plakhova, T. V.; Romanchuk, A. Y.; Gerber, E.; Weiss, S.; Efimenko, A.; Sahle, C. J.; Butorin, S. M.; Kalmykov, S. N.; Kvashnina, K. O. Understanding the Size

Effects on the Electronic Structure of ThO2 Nanoparticles. *Phys. Chem. Chem. Phys.* **2019**, *21* (20), 10635–10643. https://doi.org/10.1039/C9CP01283D.

(19) Sutter, E.; Sutter, P. Size-Dependent Room Temperature Oxidation of In Nanoparticles. *J. Phys. Chem. C* **2012**, *116* (38), 20574–20578. https://doi.org/10.1021/jp305806v.

(20) Walter, O.; Popa, K.; Blanco, O. D. Hydrothermal Decomposition of Actinide(IV) Oxalates: A New Aqueous Route towards Reactive Actinide Oxide Nanocrystals. *Open Chemistry* **2016**, *14* (1), 170–174. https://doi.org/10.1515/chem-2016-0018.

(21) Popa, K.; Walter, O.; Blanco, O. D.; Guiot, A.; Bouëxière, D.; Colle, J.-Y.; Martel, L.; Naji, M.; Manara, D. A Low-Temperature Synthesis Method for AnO2 Nanocrystals (An = Th, U, Np, and Pu) and Associate Solid Solutions. *CrystEngComm* **2018**, *20* (32), 4614–4622. https://doi.org/10.1039/C8CE00446C.

(22) Vălu, S.-O.; Bona, E. D.; Popa, K.; Griveau, J.-C.; Colineau, E.; Konings, R. J. M. The Effect of Lattice Disorder on the Low-Temperature Heat Capacity of (U 1−y Th y)O 2 and 238 Pu-Doped UO 2. *Sci Rep* **2019**, *9* (1), 1–10. https://doi.org/10.1038/s41598-019-51476-3.

(23) Petříček, V.; Dušek, M.; Palatinus, L. Crystallographic Computing System JANA2006: General Features. *Zeitschrift für Kristallographie - Crystalline Materials* **2014**, *229* (5), 345–352. https://doi.org/10.1515/zkri-2014-1737.

(24) Glatzel, P.; Bergmann, U. High Resolution 1s Core Hole X-Ray Spectroscopy in 3d Transition Metal Complexes—Electronic and Structural Information. *Coordination Chemistry Reviews* **2005**, *249* (1), 65–95. https://doi.org/10.1016/j.ccr.2004.04.011.

(25) Zimina, A.; Dardenne, K.; Denecke, M. A.; Grunwaldt, J. D.; Huttel, E.; Lichtenberg, H.; Mangold, S.; Pruessmann, T.; Rothe, J.; Steininger, R.; Vitova, T. The CAT-ACT Beamline

at ANKA: A New High Energy X-Ray Spectroscopy Facility for CATalysis and ACTinide Research. *J. Phys.: Conf. Ser.* **2016**, *712*, 012019. https://doi.org/10.1088/1742-6596/712/1/012019.

(26) Zimina, A.; Dardenne, K.; Denecke, M. A.; Doronkin, D. E.; Huttel, E.; Lichtenberg, H.; Mangold, S.; Pruessmann, T.; Rothe, J.; Spangenberg, Th.; Steininger, R.; Vitova, T.; Geckeis, H.; Grunwaldt, J.-D. CAT-ACT—A New Highly Versatile x-Ray Spectroscopy Beamline for Catalysis and Radionuclide Science at the KIT Synchrotron Light Facility ANKA. *Review of Scientific Instruments* **2017**, *88* (11), 113113. https://doi.org/10.1063/1.4999928.

(27) Glatzel, P.; Weng, T.-C.; Kvashnina, K.; Swarbrick, J.; Sikora, M.; Gallo, E.; Smolentsev, N.; Mori, R. A. Reflections on Hard X-Ray Photon-in/Photon-out Spectroscopy for Electronic Structure Studies. *J. Electron Spectrosc. Relat. Phenom.* **2013**, *188*, 17–25. https://doi.org/10.1016/j.elspec.2012.09.004.

(28) Kvashnina, K. O.; Butorin, S. M.; Martin, P.; Glatzel, P. Chemical State of Complex Uranium Oxides. *Phys. Rev. Lett.* **2013**, *111* (25), 253002. https://doi.org/10.1103/PhysRevLett.111.253002.

(29) Epifano, E.; Naji, M.; Manara, D.; Scheinost, A. C.; Hennig, C.; Lechelle, J.; Konings, R. J. M.; Guéneau, C.; Prieur, D.; Vitova, T.; Dardenne, K.; Rothe, J.; Martin, P. M. Extreme Multi-Valence States in Mixed Actinide Oxides. *Communications Chemistry* **2019**, *2* (1), 1–11. https://doi.org/10.1038/s42004-019-0161-0.

(30) Martin, P.; Ripert, M.; Petit, T.; Reich, T.; Hennig, C.; D'Acapito, F.; Hazemann, J. L.; Proux, O. A XAS Study of the Local Environments of Cations in (U, Ce)O2. *J. Nucl. Mater.* **2003**, *312* (1), 103–110. https://doi.org/10.1016/S0022-3115(02)01590-8.

(31) Yamada, K.; Yamanaka, S.; Nakagawa, T.; Uno, M.; Katsura, M. Study of the Thermodynamic Properties of (U, Ce)O2. *J. Nucl. Mater.* **1997**, *247*, 289–292. https://doi.org/10.1016/S0022-3115(97)00076-7.

(32) Kim, D.-J.; Kim, Y.-S.; Kim, S.-H.; Kim, J.-H.; Yang, J.-H.; Lee, Y.-W.; Kim, H.-S. The Linear Thermal Expansion and the Thermal Diffusivity Measurements for Near-Stoichiometric (U, Ce)O2 Solid Solutions. *Thermochimica Acta* **2006**, *441* (2), 127–131. https://doi.org/10.1016/j.tca.2005.12.009.

(33) Bera, S.; Mittal, V. K.; Venkata Krishnan, R.; Saravanan, T.; Velmurugan, S.; Nagarajan, K.; Narasimhan, S. V. XPS Analysis of UxCe1−xO2±δ and Determination of Oxygen to Metal Ratio. *J. Nucl. Mater.* **2009**, *393* (1), 120–125. https://doi.org/10.1016/j.jnucmat.2009.05.015.

(34) Prieur, D.; Carvajal-Nunez, U.; Somers, J. O/M Ratio Determination and Oxidation Behaviour of Th0.8Am0.20O2-x. *J. Nucl. Mater.* **2013**, *435* (1–3), 49–51. https://doi.org/10.1016/j.jnucmat.2012.12.011.

(35) Desfougeres, L.; Welcomme, É.; Ollivier, M.; Martin, P. M.; Hennuyer, J.; Hunault, M. O. J. Y.; Podor, R.; Clavier, N.; Favergeon, L. Oxidation as an Early Stage in the Multistep Thermal Decomposition of Uranium(IV) Oxalate into U3O8. *Inorg. Chem.* **2020**. https://doi.org/10.1021/acs.inorgchem.0c01047.

(36) Manaud, J.; Maynadié, J.; Mesbah, A.; Hunault, M. O. J. Y.; Martin, P. M.; Zunino, M.; Meyer, D.; Dacheux, N.; Clavier, N. Hydrothermal Conversion of Uranium(IV) Oxalate into Oxides: A Comprehensive Study. *Inorg. Chem.* **2020**, *59* (5), 3260–3273. https://doi.org/10.1021/acs.inorgchem.9b03672.

(37) Paun, C.; Safonova, O. V.; Szlachetko, J.; Abdala, P. M.; Nachtegaal, M.; Sa, J.; Kleymenov, E.; Cervellino, A.; Krumeich, F.; van Bokhoven, J. A. Polyhedral CeO2 Nanoparticles: Size-Dependent Geometrical and Electronic Structure. *J. Phys. Chem. C* **2012**, *116* (13), 7312–7317. https://doi.org/10.1021/jp300342b.

(38) Bianconi, A.; Marcelli, A.; Dexpert, H.; Karnatak, R.; Kotani, A.; Jo, T.; Petiau, J. Specific Intermediate-Valence State of Insulating 4f Compounds Detected by ${L}_{3}$ x-Ray Absorption. *Phys. Rev. B* **1987**, *35* (2), 806–812. https://doi.org/10.1103/PhysRevB.35.806.

(39) Soldatov, A. V.; Ivanchenko, T. S.; Kotani, A.; Bianconi, A. L3 Edge X-Ray Absorption Spectrum of CeO2: Crystal Structure Effects. *Physica B: Condensed Matter* **1995**, *208–209*, 53–55. https://doi.org/10.1016/0921-4526(94)00633-7.

(40) Cafun, J.-D.; Kvashnina, K. O.; Casals, E.; Puntes, V. F.; Glatzel, P. Absence of Ce3+ Sites in Chemically Active Colloidal Ceria Nanoparticles. *ACS Nano* **2013**, *7* (12), 10726–10732. https://doi.org/10.1021/nn403542p.

(41) Vitova, T.; Denecke, M. A.; Goettlicher, J.; Jorissen, K.; Kas, J. J.; Kvashnina, K.; Pruessmann, T.; Rehr, J. J.; Rothe, J. Actinide and Lanthanide Speciation with High-Energy Resolution X-Ray Techniques. In *15th International Conference on X-Ray Absorption Fine Structure (xafs15)*; Wu, Z. Y., Ed.; Iop Publishing Ltd: Bristol, 2013; Vol. 430, p UNSP 012117.

(42) Butorin, S. M.; Kvashnina, K. O.; Smith, A. L.; Popa, K.; Martin, P. M. Crystal-Field and Covalency Effects in Uranates: An X-Ray Spectroscopic Study. *Chem. Eur. J.* **2016**, *22* (28), 9693–9698. https://doi.org/10.1002/chem.201505091.

(43) Popa, K.; Prieur, D.; Manara, D.; Naji, M.; Vigier, J.-F.; Martin, P. M.; Blanco, O. D.; Scheinost, A. C.; Pruessmann, T.; Vitova, T.; Raison, P. E.; Somers, J.; Konings, R. J. M.

Further Insights into the Chemistry of the Bi-U-O System. *Dalton Trans.* **2016**, *45* (18), 7847–7855. https://doi.org/10.1039/c6dt00735j.

(44) Butorin, S. M.; Kvashnina, K. O.; Prieur, D.; Rivenet, M.; Martin, P. M. Characteristics of Chemical Bonding of Pentavalent Uranium in La-Doped UO2. *Chem. Comm.* **2017**, *53* (1), 115–118. https://doi.org/10.1039/c6cc07684j.

(45) Pidchenko, I.; Kvashnina, K. O.; Yokosawa, T.; Finck, N.; Bahl, S.; Schild, D.; Polly, R.; Bohnert, E.; Rossberg, A.; Goettlicher, J.; Dardenne, K.; Rothe, J.; Schaefer, T.; Geckeis, H.; Vitova, T. Uranium Redox Transformations after U(VI) Coprecipitation with Magnetite Nanoparticles. *Environ. Sci. Technol.* **2017**, *51* (4), 2217–2225. https://doi.org/10.1021/acs.est.6b04035.

(46) Kauric, G.; Walter, O.; Beck, A.; Schacherl, B.; Dieste Blanco, O.; Vigier, J.-F.; Zuleger, E.; Vitova, T.; Popa, K. Synthesis and Characterization of Nanocrystalline U1-XPuxO2(+y) Mixed Oxides. *Materials Today Advances* **2020**, *8*, 100105. https://doi.org/10.1016/j.mtadv.2020.100105.

(47) Shannon, R. D. Revised Effective Ionic Radii and Systematic Studies of Interatomic Distances in Halides and Chalcogenides. *Acta Cryst A, Acta Cryst Sect A, Acta Crystallogr A, Acta Crystallogr Sect A, Acta Crystallogr A Cryst Phys Diffr Theor Gen Crystallogr, Acta Crystallogr Sect A Cryst Phys Diffr Theor Gen Crystallogr* **1976**, *32* (5), 751–767. https://doi.org/10.1107/S0567739476001551.

(48) Razdan, M.; Shoesmith, D. W. Influence of Trivalent-Dopants on the Structural and Electrochemical Properties of Uranium Dioxide (UO2). *J. Electrochem. Soc.* **2013**, *161* (3), H105. https://doi.org/10.1149/2.047403jes.

(49) Kim, J.-G.; Ha, Y.-K.; Park, S.-D.; Jee, K.-Y.; Kim, W.-H. Effect of a Trivalent Dopant, Gd3+, on the Oxidation of Uranium Dioxide. *J. Nucl. Mater.* **2001**, *297* (3), 327–331. https://doi.org/10.1016/S0022-3115(01)00639-0.

(50) Herrero, B.; Bès, R.; Audubert, F.; Clavier, N.; Hunault, M. O. J. Y.; Baldinozzi, G. Charge Compensation Mechanisms in Nd-Doped UO2 Samples for Stoichiometric and Hypo-Stoichiometric Conditions: Lack of Miscibility Gap. *J. Nucl. Mater.* **2020**, *539*, 152276. https://doi.org/10.1016/j.jnucmat.2020.152276.

(51) Caisso, M.; Roussel, P.; Den Auwer, C.; Picart, S.; Hennig, C.; Scheinost, A. C.; Delahaye, T.; Ayral, A. Evidence of Trivalent Am Substitution into U3O8. *Inorg Chem* **2016**, *55* (20), 10438–10444. https://doi.org/10.1021/acs.inorgchem.6b01672.

(52) Bes, R.; Rivenet, M.; Solari, P.-L.; Kvashnina, K. O.; Scheinost, A. C.; Martin, P. M. Use of HERFD-XANES at the U L-3- and M-4-Edges To Determine the Uranium Valence State on [Ni(H2O)(4)](3)[U(OH,H2O)(UO2)(8)O-12(OH)(3)]. *Inorg. Chem.* **2016**, *55* (9), 4260–4270. https://doi.org/10.1021/acs.inorgchem.6b00014.

(53) Epifano, E.; Vauchy, R.; Lebreton, F.; Lauwerier, R.; Joly, A.; Scheinost, A.; Guéneau, C.; Valot, C.; Martin, P. M. On the O-Rich Domain of the U-Am-O Phase Diagram. *J. Nucl. Mater.* **2020**, *531*, 151986. https://doi.org/10.1016/j.jnucmat.2020.151986.

TOC (For Table of Contents Only)

Uranium coexist in different valence states (U^{IV}, U^{V} and U^{VI}) in $(U,Ce)O_2$ fluorite structure.